

Quasi-static response and multi-objective crashworthiness optimization of oblong tube under lateral loading

A.Baroutaji^a, E.Morris^a, A.G.Olabi^b

(a) School of Mechanical and Manufacturing Engineering, Dublin City University, Glasnevin, Dublin 9, Ireland

(b) University of the West of Scotland, School of Engineering, High Street, Paisley, PA1 2BE, UK.

Abstract:

This paper addresses the energy absorption responses and crashworthiness optimisation of thin-walled oblong tubes under quasi-static lateral loading. The oblong tubes were experimentally compressed using three various forms of indenters named as the flat plate, cylindrical and a point load indenter. The oblong tubes were subjected to inclined and vertical constraints to increase the energy absorption capacity of these structures. The variation in responses due to these indenters and external constraints were demonstrated. Various indicators which describe the effectiveness of energy absorbing systems were used as a marker to compare the various systems. It was found that unconstrained oblong tube (FIU) exhibited an almost ideal response when a flat plate indenter was used. The design information for such oblong tubes as energy absorbers can be generated through performing parametric study. To this end, the response surface methodology (RSM) for the design of experiments (DOE) was employed along with finite element modelling (FEM) to explore the effects of geometrical parameters on the responses of oblong tubes and to construct models for the specific energy absorption capacity (SEA) and collapse load (F) as functions of geometrical parameters. The FE model of the oblong tube was constructed and experimentally calibrated. In addition, based on the developed models of the SEA and F, multi-objective optimization design (MOD) of the oblong tube system is carried out by adopting a desirability approach to achieve maximum SEA capacity and minimum F. It is found that the optimal design of FIU can be achieved if the tube diameter and tube width are set at their minimum limits and the maximum tube thickness is chosen.

Keywords: Energy absorbing systems, Oblong tubes, Finite element method (FEM), Quasi-static, Design of experiment (DOE), Response surfaces method (RSM), Multi-objective optimization design (MOD)

Nomenclature

e_g : crush efficiency

e_E : energy efficiency

W_{eff} : weight effectiveness

E: The energy absorption capacity

SEA: specific energy absorption capacity

F: collapse load

Abbreviations

FIU: flat plate indenter-unconstrained system.

FISC: flat plate indenter-side constraints system.

FIIC: flat plate indenter-inclined constraints system.

CIU: cylindrical indenter-unconstrained system.

CISC: cylindrical indenter-side constraints system.

CIIC: cylindrical indenter-inclined constraints system.

PIU: point indenter-unconstrained system.

PISC: point indenter-side constraints system.

PIIC: point indenter-inclined constraints system.

1 Introduction

Tubular systems which consist of one or more circular or square sectioned tubes are commonly used to absorb kinetic energy through plastic deformation.

These structural elements can absorb kinetic energy from many types of deformation leading to various energy absorption responses. The principle deformation mechanisms of tube include lateral compression, lateral indentation, axial crushing, tube splitting, and tube inversion. A significant amount of research has been conducted on the energy dissipated by tubular systems over the last three decades. The main findings were outlined and presented in a research article by Olabi et al. [1] and Alghamdi [2].

The lateral compression of circular tube were analysed by DeRuntz and Hodge [3], flat plate indenter was used to compress the tubes. The authors used rigid perfectly plastic material model to predict the force-deflection response of the tube. They found that the collapse load is affected by the geometrical factors and material properties of the tube. Reid and Reddy [4] performed further investigations on strain hardening effects. They developed an accurate material model which considered both geometric and material strain hardening effects. The authors reported that the energy absorbing capacity can be maximised by choosing appropriate tube dimensions.

Gupta et al [5] examined numerically and experimentally the lateral crushing of circular metallic tubes under quasi-static conditions. Aluminium and mild steel tubes with different diameter to thickness ratios were used in this investigation. The authors found that the energy absorbing capacity and mean collapse load increases with increase in thickness and decrease in diameter.

Increasing the energy absorption capacity of the tubular system by means of external constraints was applied by Reddy and Reid [6]. The authors built a tubular system with side constraints in which the horizontal diameter of the tube was prevented from translating laterally. It was found that the energy absorbed by a system with side constraints was three times more than the system with no constraints.

The application of inclined constraints as an alternative to vertical ones also increases the energy absorbing capacity of tubes/rings. Reid [7] studied the effect of varying the inclination angle for the lateral compression of tubes. In general it was concluded that an externally constrained system is a viable method to increase its energy absorbing capacity.

The above studies were concerned with the compression of tubes under rigid platens. However, alternative ways of compressing these systems are possible by incorporating point-load indenters as

shown by Reid and Bell [8]. The load deflection for this type of compression tends to be unstable once the collapse load has been reached. This behaviour is termed deformation softening as opposed to deformation-hardening.

Instead of using flat plate or point-load indenter, Shim and Stronge [9] used cylindrical indenters to compress ductile, thin walled tubes. The authors investigated the post-collapse response of these tubes. The unstable response was also noticed for this kind of indenter.

In addition to circular tubes, various geometry shapes of tubes have been proposed by researchers to use as energy absorbers under lateral loading such as elliptical tubes [10, 11] and oblong tubes [12].

Recently, researchers have utilized the finite element method (FEM) to predict the responses of energy absorption systems under quasi-static [12, 13] and dynamic [14, 15] lateral loading. Morris et al. [13] employed ANSYS to predict the responses of nested circular tubes compressed by two types of indenters and subjected to external constraints. Close agreements between the computational and experimental results were obtained.

Another numerical technique which is response surfaces method (RSM) was employed by researchers to seek an optimal design and to perform the multi-objective optimization design (MOD) of energy absorption system under pure axial [16, 17], lateral [18] and oblique loads [19].

Much of the research on thin-walled tube energy absorbers crushed laterally has focused on those of circular cross section. However, the oblong tubes which are a modified form of circular tubes have received less attention. In the present work, the oblong tubes are proposed as energy absorption components. These tubes are expected to have high energy absorptions performance as they have a greater lateral displacement stroke compared with circular tube systems. The crushing responses of these tubes under quasi-static lateral loading have been investigated experimentally. The lateral compressions were applied through three types of indenters named as flat plate, cylindrical, and point-load indenter. Different variations of external constraints were incorporated into the oblong tube energy absorption system to increase the energy absorption capacity of these systems. In addition, with the aim of generating the design guidelines for such oblong tube as energy absorbing devices under lateral loading, the response surface method (RSM) for design of experiments (DOE) was used in conjunction with the finite element modelling (FEM). The FE model was developed using

commercial finite element code (ANSYS) and validated using experimental techniques. The specific energy absorption capacity (SEA) and the collapse load (F) of the oblong tube were modelled as functions of geometrical parameters such as thickness (t), diameter (D), and width (W). Factorial study was performed to investigate the primary and interaction effects of geometric parameters on the specific energy absorbed and collapse load. Furthermore, Based on the developed models of the SEA and F, the approach of multi-objective optimization design was applied to find the optimal configuration of the oblong tube.

2 Experimental work

2.1 Material and Geometrical properties

Mild Steel tubes were used in this work. The tubes were cold finished, manufactured according to the DIN standards (DIN 2393 ST 37.2) and containing around 0.15% carbon. Tensile tests were carried out in order to determine the mechanical properties of the tubes as shown in Figure 1. Figure 1 displays the true stress-strain curve of the tensile sample. Upon examination of this figure, it can be seen that the stress-strain curve displays unusual behaviour in which strain softening occurred almost immediately after yielding with no evidence of strain hardening. This phenomenon is due to sample necking which takes place immediately after yielding. This behaviour is termed as tension instability and the cold rolling process might be the reason for this. Table 1 shows the mechanical properties of the mild steel material derived from the true stress-strain curve and used in the FE modelling. The yield stress is validated according to DIN standards, which state that the yield stress of this material is within the range of 450–525MPa [13, 14]. A non-zero value of 1500 MPa was employed to represent the hardening modulus of this material. The same value of hardening modulus was used by [14, 15] to define the softening stage of the same material.

2.2 Experimental set-up

The Instron Model 4204 testing machine was used to perform the quasi-static experiments on the samples studied. The loading force was measured by load cell which was attached to the moving crosshead of the loading frame. The Instron accompanying software was used to control the crosshead movement along with providing the data acquisition and results from the loading frame. A prescribed slow velocity of 10 mm/min was applied to the moving crosshead of the instrument to ensure that there were no dynamic effects. Many researchers [12, 13] used velocities between 0.5 and 15 mm/min in the quasi-static lateral compression tests. The quasi-static test set-up for oblong tube sample is shown schematically in Figure 2.

2.3 Oblong Tube Specimen Preparation

Using suitable fixtures, an oblong curve profile was generated by subjecting a cylindrical tube to opposing tension forces, as shown in Figure 3. A displacement of 40 mm was applied to a circular tube test piece with outer diameter of 101.6 mm, thickness of 3.25 mm and width of 40 mm, this value is the maximum extension distance that can be applied to a given circular tube as any further increase in the elongation distance might cause the formation of plastic hinges at the horizontal line of the tube, and hence buckling inwards would occur. This elongation distance value was also used by Olabi et al. [13]. Figure 4 shows the force-deflection response of a test piece during the tensile loading phase. The objective is to load the tube plastically so that extra displacement during the compression phase can be achieved. This allows for more energy to be absorbed for the same mass.

2.4 Experimental results and discussion

2.4.1 Experimental results comparison of oblong and circular tubes under lateral loading

To prove the crash resistance advantages of the oblong system, a comparison of the crush behaviour of the oblong and circular tubes has been performed. The force-deflection responses for the circular

and oblong tubes under quasi-static loading are shown in Figure 5 . The tubes were crushed up to 70 % of their original diameter/height to avoid the self-contact of the tube.

It can be clearly seen that the oblong tube has a longer crushing stroke which is around 30 % more than the circular tube. The circular and oblong tubes have almost the same magnitude of collapse load while the post collapse stage is more stable and almost constant in the oblong tube. The constant force-deflection response of the oblong tube is due to residual stresses created during the forming of the oblong tube specimen. The Table 2 shows the comparison of oblong and circular tubes in terms of energy absorption capacity and specific energy absorption capacity. It can be seen that the oblong tube can absorb around 35% energy more than the circular tube.

Overall, it is clear from the above comparison that the oblong tubes display several key advantages over circular tubes for absorbing energy under lateral loading, as follows:

- Oblong tubes display a more stable and almost constant force-deflection response in the post collapse stages.
- The energy absorption capacity of oblong tubes is greater than that for circular tubes of equivalent mass.

2.4.2 Experimental results of oblong tube compressed by different indenters and exposed to external constraints

2.4.2.1 Flat plate indenter

Figure 6 and Figure 7 illustrate the force and energy absorption responses and the stages of compression for the FIU system. The force increases rapidly up to its characteristic ‘collapse’ load followed by a slight strain softening response. This softening stage is due to the oblong curve profile generated during the preparation/loading phase. The elongation of a circular tube plays a role in generating a larger moment arm from the point of load application to the horizontal hinge points in the post stages of the collapse. As a result less force is required to maintain the deformation. At approximately 60 mm deflection, the force begins to rise. This is due to the points of contact

continually moving away from the centre between the upper plate and the oblong structure. This results in a shorter moment arm, which therefore requires a greater force to continue or sustain the deformation process. Since the tube is elongated in the vertical direction, the potential displacement stroke is increased. In order to avoid a system overload that may cause the tube to fracture, the responses of all systems were calculated up to 100 mm (70% of oblong tube length), as shown in Figure 7. It can be noticed from Figure 6 that an almost constant crushing force is achievable in the FIU system, which is a desirable feature in energy absorbing systems.

External inclined constraints at an angle 15 degrees were used to create FIIC. The Figure 8 displays the force and energy responses of the FIIC system along with the various stages of deformation in Figure 9. It can be seen from that similar responses to unconstrained tests were obtained, but with an increase in resulting force being observed in the post collapse stages. This increase was due to the presence of the constraints resulting in more volume of the material being subjected to deformation, as reported by Reid [7].

Figure 10 depicts the crush force and energy absorption for an FISC system. A smaller flat indenter is incorporated in this system as there was limited width availability after installing the side constraints, as seen in Figure 11. It is possible to choose an indenter equal to the available width. However this brings its own complications in the sense that a very large load would be required to compress the system, which may exceed the limit of the load cell. At approximately 60mm deflection, the force increases due to the presence of the side constraint preventing the horizontal diameter of the oblong specimen from moving laterally and thus exposing more material to plastic deformation. A similar observation was reported by [6], where side constraints were used during the compression of circular tube. From approximately 70mm, the peak force drops briefly and rises again and then continues dropping. The slight oscillation in force noticed at 70 mm is due to additional plastic hinges being formed between the edge of the indenter and the test piece, as shown in Figure 11.

2.4.2.2 Cylindrical indenter

Figure 12 displays the force and energy response for a CIU system. When the crush force is reached,

the system begins to strain soften. This is an unstable deformation characteristic and is due to the moment arm increasing and thus requiring less compressive force to maintain the compression stroke. Due to the design of the cylindrical indenter, a higher stroke length can be obtained in systems that use this indenter configuration. At approximately 80 mm, more strain softening was noticed due to partial structural failure occurring at the top plastic hinge, as shown in Figure 13.

Figure 14 and Figure 15 illustrate results for a CIIC system. A slight increase in the resulting force occurs due to the presence of the inclined constraints. Similar to the CIU system, the CIIC system exhibits unstable behaviour and partial structural failure (Figure 15). The responses of the CISC system are presented in Figure 16 and Figure 17. When contact was established between the test piece and the side constraints, an increase in force was observed due to the prevention of the horizontal diameter of the test piece being deflected, thereby inducing additional plastic hinges. These additional hinges required extra force in order to overcome local plastic deformation. A significant increase in load was noticed towards the end of the displacement stroke for both CIIS and CISC. This increase was due to the oblong tube conforming to the shape of the cylindrical indenter, as shown in Figure 15 and Figure 17, and also due to material strain hardening characteristics.

2.4.2.3 Point indenter

(Figure 18, Figure 19, Figure 20, Figure 21, Figure 22, and Figure 23) illustrate the force and energy responses of test specimens being compressed using a point indenter. The responses of these specimens are very similar to those specimens compressed using cylindrical indenters. In all systems (PIU-PIIC-PISC) at approximately 60 mm deflection, complete structural failure occurs due to excessive plastic deformation occurring in a very localised region at the point of load application (Figure 24).

2.5 Energy absorber characteristics

The performance of energy absorbing systems can be evaluated by means of several criteria. Some useful indicators were proposed by Thornton et al. [20], such as crush efficiency, energy efficiency,

specific energy absorption capacity, and weight effectiveness. The specific energy absorption capacity is the most important characteristic of energy absorbers. SEA is defined by energy absorbed per unit mass, and is given by:

$$SEA = \frac{E}{m} \quad (1)$$

Where m is the mass of the energy absorber. E is the energy absorption capacity which can be measured by calculating the area under the force-deflection response of an energy absorbing device. The energy absorption capacity can be defined as the integration of a load-displacement curve as follow.

$$E = \int_0^{\delta} F(\delta) \cdot d\delta \quad (2)$$

Where δ is the displacement, and $F(\delta)$ is the load-displacement response.

The stroke efficiency is defined as the stroke length divided by the characteristic length of a structure, such as the outer diameter or the original length. The stroke efficiency for lateral collapse of a oblong tube can be defined by the equation

$$e_g = \frac{\delta}{L} \quad (3)$$

Where L is the major axis length of oblong tube, e_g is considered as a good indicator for describing the amount of material that can be used during collapse.

The energy efficiency indicator is given by

$$e_E = \frac{E}{F_{max} * L} \quad (4)$$

Where F_{max} is the maximum load observed in the force-displacement response, and L is the original length of the absorber. It is recommended to maximize the energy efficiency of the energy absorber. Ideally, to achieve the maximum value of e_E , the force-displacement response of the energy absorber should be a rectangle response.

The work effectiveness is a combination of the specific energy absorption capacity and the crush efficiency indicator, and it is defined as follow:

$$W_{eff} = SEA \times e_g \quad (5)$$

This indicator is a very useful one, particularly in structures that are restricted in terms of both weight and space. Figure 25 presents the various indicators (e_g , e_E , W_{eff}) for all oblong tube systems. The oblong tubes compressed by flat plate indenters (FIU-FIIC-FISC) presented the best efficiencies, while the point indenter systems (PIU-PIIC-PISC) resulted in low efficiencies. The maximum energy efficiency was obtained from the FIU system due to its response characteristics exhibiting a rectangular or constant crushing force throughout its loading phase. The maximum weight effectiveness was obtained by FISC due to a larger amount of specific energy absorbed by it. This observation was also noticed for circular tubes compressed by flat indenter and exposed to side constraints as reported by [6].

From the results shown above, it appears that the FIU system showed a better performance in terms of (e_g , e_E) under lateral loading, compared with the other systems configurations. Moreover, the FIU has the simplest design and an almost optimal force-deflection response. The FIU system was thus selected as the best energy absorption system in the oblong tubes category. In the following sections, the influences of important geometric parameters on the crushing response of FIU tubes are first examined by means of a parametric study, followed by a multi-objective optimization design (MOD) to further improve its crashworthiness under lateral loading.

3 Numerical Simulations

3.1 Finite element model

Finite element techniques were used to predict the deformation behaviour of FIU system. Figure 26 displays the finite element model used to simulate the responses of this system. A 3D-structural solid element (solid 45) which has eight nodes with large strain, large deflection and plasticity capabilities

was used to model the oblong profile. The Flat indenter was modelled as rigid body and constrained to move vertically along the vertical y axis. The base was also modelled as a rigid entity with all rotations and translations being fixed. A bilinear isotropic hardening material model was employed to define the material behaviour of the system. The yield stress and plastic modulus, the latter which describes the plastic portion of the stress-strain curve were determined from the tensile test as listed in Table 1. The contact algorithm employs a non-linear ‘surface to surface’ formulation to define contact between various interacting surfaces. An augmented Lagrangian penalty option with friction coefficient value of 0.2 was employed in all contact pairs. All models were subjected to symmetry boundary conditions in order to reduce simulation solve times. Large strain – deformation was included in the finite element model due to the test specimen which experiences significantly high displacement.

3.2 Mesh convergence

Figure 27 shows the convergence graph of six different mesh densities. Convergence was obtained when an element length of 2 mm or less was used to mesh the specimen geometry profile. This element size is used in all subsequent prediction models in this study.

3.3 Geometry creation of the oblong shaped tubes

The profile of the oblong specimen was obtained by applying the same load and boundary condition as used in the experiments. A displacement of 40 mm was applied to a circular tube with an outer diameter of 101.6 mm, thickness of 3.25 mm, and width of 40 mm. Figure 28 shows the initial and final stages of tensile displacement. This newly formed oblong profile was then used as a finite element model for subsequent analysis.

3.4 Numerical results and validation of FE model

Figure 29 shows the predicted and experimental force-deflection and energy-deflection curves for compression of an oblong tube under a flat indenter. Figure 30 illustrates the initial and final deformed shape of FIU simulation model. Comparison of simulation and experimental

results illustrates that the collapse load is in close agreement. This is indicative of the predicted model being sufficiently accurate in capturing the position of the localised hinges. However, in the post collapse stages the predicted results tend to underestimate the force-deflection, followed by a slight over-estimation towards the end of the displacement stroke.

The slight discrepancy may be due to a number of reasons. Firstly, recall that the oblong tube was prepared by subjecting it to tensile loads as outlined earlier. It is possible that the force deflection response is very sensitive to the final curvature of this profile. A slight difference between the profile used in the experiment, and that predicted by the finite element model, may result in differences during the post collapse stage of loading. In addition, recall that the material stress strain curve used in this study exhibits an unusual ‘material’ strain softening phenomena which characterises a negative slope. This type of material behaviour cannot be accounted for in the bilinear material prediction model since it requires that the data points generate a slope greater than zero. Therefore, it is possible that the finite element model’s ability to capture the ‘material’ strain softening phenomena with sufficient accuracy is limited. Table 3 shows the comparison of experimental and predicted values of SEA and F for the FIU system. From the comparison showed in Table 3 and Figure 29, it can be seen that all of the numerical results are in excellent agreement with the experimental results. This agreement indicated that the FE model is valid.

4 Response surface models and parametric study of FIU system

4.1 Sampling design points (Experimental design)

An experimental design was created based on a three level Box–Behnken design with full replication [21]. Tube widths (W) ranging between 10 and 60 mm, tube outer diameters (D) between 8 and 130 mm, and tube thicknesses (t) between 2.5 and 6 mm were applied as independent input variables. Table 4 shows the specific values used in the experiments. These dimensions were chosen as they covered the typical range of tube sizes commonly used in crashworthiness applications. The specific energy absorbed (SEA) and collapse load (F) were selected as design responses. The oblong tube

models were prepared by the elongation method as described earlier. A ratio of 2.54 between the outer diameter of the circular tube and the elongation distance was used to create the oblong tube models. This same ratio was used by [13]. The SEA responses for all models have been calculated up to 70% of the oblong tube length.

4.2 Development of RS models

Response surface methodology (RSM) was applied using statistical software, Design-expert V8 [24], to the numerical data obtained based on the finite element model described earlier which has been validated in Figure 29 and Table 3. Numerical simulations were performed for the different combinations of independent variables provided by the DOE software. The design responses were calculated for each combination of design variables. The different combinations of design variables with corresponding design responses are tabulated in Table 5. Highest order polynomials were suggested by DOE to obtain the regression equations where the additional terms are insignificant and the model is not aliased. A step-wise regression method was used to fit the polynomial equation to the experimental data and to identify the relevant model terms [22, 23, and 25]. The sequential F-test for significance of both the regression model and the individual model terms along with the lack of fit test were carried out using Design-Expert V8. The same statistical software was used to generate the statistical and response plots.

The resulting ANOVA tables (Table 6 and Table 7) have been created for the SEA and F Models. These tables summarize the analysis of variance for each response and show the significant model terms. The F-value of both models indicates that the models are significant with only 0.01% chance such that the “Model F-value” could have occurred due to noise. The same tables show the other adequacy measures R², adjusted R² and predicted R². The predicted R squared and the adjusted R-squared are within 0.20 of each other, which agrees with what it is stated in [24]. The adequate precision ratio compares the range of the predicted value at the design points to the average prediction error. In all cases the value of adequate precision are significantly greater than 4. The adequate precision ratio above 4 indicates an adequate signal. This means that the model can be used to navigate the design space. The analysis of variance indicates that most significant terms associated

with specific energy absorbed are the first order effect of thickness (t) and diameter (D).

While, for the crush load model, the analysis of variance indicated that the most significant terms are:

1. The first order effect of tube diameter (D), tube thickness (t) and tube width (W).
2. The second order effect of tube thickness (t) and tube width (W).
3. The two level of interaction between the tube thickness and the tube width (t-w).

The final mathematical models in terms of actual factors as determined by the design expert software for the SEA and F are shown in Table 6 and Table 7 respectively.

4.3 Validation of the RS models

Figure 31 and Figure 32 show the relationship between the actual and predicted values of specific energy absorbed and mean force, respectively. These figures indicate that the developed RS models are adequate, because the residuals in the prediction of each response are small since most of SEA and F values lie on the best-fit line of the predicted results. Furthermore, to verify the adequacy of the developed RS models, a comparison between the numerical, experimental, and predicted responses was performed. Using the point prediction option in the DOE software, the specific energy absorbed and collapse load of the validation experiments were predicted using the previous developed models. Table 8 presents the experimental condition, the actual values, the numerical values, the predicted values, and the percentages of error. It can be seen that all of the percentage errors are within the acceptable tolerances and this indicate that the RS models are validated.

4.4 Parametric study

4.4.1 Effect of geometrical factors on SEA response

The perturbation plot of SEA shown in Figure 33 indicates that the SEA depended mainly on the thickness and diameter of the tube. The insignificant effect of the width on the SEA has been eliminated by the software package.

Figure 34 shows the effect of tube diameter (D) on SEA. It is seen that SEA decreases as the tube diameter increases. This behaviour was also noticed for circular tubes [5]. This behaviour is probably due to localization of plastic strain around the plastic hinges that reduce the volume of material subjected to plastic deformation in the larger tubes. In addition, the increased weight in the larger tubes made the energy absorbed per unit mass (SEA) lower.

Figure 35 displays the effect of tube thickness on the SEA. Obviously, it can be noticed that SEA increased as the thickness increased. This phenomenon is due to fact that the thicker tubes have more material available for plastic deformation.

Figure 36 shows the variation of SEA with diameter and thickness, it can be seen that a greater amount of SEA can be absorbed if smaller and thicker tubes were used.

4.4.2 Effect of Geometrical factors on F response

The effect of tube diameter on the crush force is presented in Figure 37. It can be noticed that the crush force decreased with increasing of tube diameter. The resistance of larger tubes to lateral collapse is lower than in the case of the smaller tubes, so lower reaction forces can be obtained in the larger tubes. This behaviour is due to smaller tubes have a shorter moment arm from the point of load application to the horizontal hinge points. Therefore a greater magnitude of force was required to initiate the collapse in the smaller tubes. This effect was found to be consistent with the effect of circular tube diameter on its collapse load, as addressed by [3 and 5].

Figure 38 shows the interaction effect of width and thickness on the collapse load (F). A two-factor interaction effect occurs when the effect of a first factor on the design response depends on the setting of the second factor. From Figure 38, it can be seen that the effect of tube thickness on F is dependent on the tube width. The effect of thickness on F is more significant in the wider tubes. It can be reported that thicker and longer oblong tubes require a higher load to initiate lateral collapse due to the greater amount of material across the section of the tube. The same observation was reported by [3] for the lateral collapse of circular tubes.

Figure 39 shows the variation of F with thickness and width. It can be seen that the minimum magnitude of F was obtained when the minimum magnitude of width was chosen.

5 Multi-objective optimization design (MOD) of FIU system

5.1 MOD approach

In crashworthiness design, the energy-absorption capacity of a thin-walled tube is evaluated by means of the specific energy absorption (SEA), which is the energy absorbed per unit mass of a thin-walled tube. Therefore, the main objective of this optimum design is to maximize the SEA.

On the other hand, and based on human safety issues, the collapse load (F) should not exceed a certain criterion. Thus the collapse load (F) can be set and minimized as another objective function. A multi-objective design can be drawn up based on the RS models constructed in section 4.3. The multi-objectives of this design are aimed at achieving the maximum SEA and to minimize the value of the collapse load (F). The values of diameter D, thickness t, and width W were set to vary in order to seek the optimal configuration of the tube. Equal importance was assigned for both objectives but a more emphasis was given to the SEA objective by specifying the maximum weight for it. Therefore, the MOD problem of oblong tube under lateral loading can be formulated as follow:

$$\begin{cases} \text{Maximize } f1 = SEA(x) \\ \text{Minimize } f2 = F(x) \\ \text{s.t. } x^l \leq x \leq x^u \end{cases}$$

Where $x = (x_1, x_2, \dots, x_k)$ are the vector of k design variables, $x^l = (x^l_1, x^l_2, \dots, x^l_k)$ and $x^u = (x^u_1, x^u_2, \dots, x^u_k)$ are respectively the lower and upper bounds of the design variables.

The design variable limits and responses objectives of the MOD are listed in Table 9.

5.2 Optimization algorithm:

There are different statistical techniques that solve multiple response problems. These include, overlaying the contour plots for each response, constrained optimization problems, and the desirability approach. The desirability method is recommended due to its simplicity, availability in the design-expert software, and because it offers flexibility in weighting and can assign different

importance values for individual responses. Solving multiple response optimization problems using the desirability method involves using a technique for combining multiple responses into a dimensionless measure of performance called the overall desirability function. In particular, the desirability approach involves transforming each estimated response into a unit-less utility bounded by $0 < d_i < 1$, where a higher d_i value indicates that response value is more desirable [24]. The numerical optimization feature in the Design expert V8 software package searches for one or more points in the factors domain that will maximize the desirability function.

5.3 Results and discussions

The Table 10 shows the geometrical factors that lead to a maximized SEA and minimized F. The best desirability were achieved when the tube diameter and tube width were set at their minimum limit (80 mm, 10 mm), and the maximum tube thickness (6 mm). So it can be reported that the thicker, shorter, and smaller oblong tubes are more appropriate for crashworthiness applications.

5.4 Graphical optimization

The graphical optimization results allow visual inspection to choose the optimum geometrical factors [24]. For each response, the lower and upper limits have been selected according to the numerical optimization results. The same criteria, which are proposed in the numerical optimization, were explained in the graphical optimization. The blank areas on the overlay plots in Figure 40 are the regions that do not meet the proposed criteria.

5.5 Confirmations

Numerical simulation was performed with the optimized conditions in order to valid the optimized results. The Table 11 shows the comparison between the numerical results and the predicted results. The geometrical shape and the responses of optimal solutions are also displayed in Table 11. It can be seen that the numerical results offered by FE (ANSYS) are in reasonable correlation with the predicted results offered by RSM (DOE).

6 Conclusion

The quasi-static responses of oblong tubes compressed with three different indenters and exposed to external constraints have been experimentally examined. Based on validated FE model, parametric studies and multi-objective optimization design have been established by using DOE results.

The main points concluded from this study are summarised below:

- Oblong tubes present an almost ideal response when a flat plate indenter is used.
- The maximum efficiency was obtained from the FIU system due to its ideal response and the maximum value of weight effectiveness was offered by FISC system due to a larger amount of specific energy absorbed by it.
- The systems compressed under cylindrical and point indenters produced unstable deformation characteristics due to strain-softening phenomena noticed in the post-collapse stage of the load-displacement curves. Smaller crush and energy efficiencies were obtained by these systems because of the tendency for complete fracture to occur at the point of applied load.
- Exposing the oblong tube systems to external constraints allowed more volume of the oblong tube to be deformed and increase the specific energy absorbed by the tube.
- The tube geometry was found to have significant effects on responses of FIU system. It was noticed that the smaller and thicker tubes have higher SEA and F. Insignificant effect of tube width on SEA has been reported. Increasing of tube width leads to increase the crush force.
- From the optimization study it was found that the optimal design of FIU can be achieved if tube diameter and tube width were set at their minimum limit and the maximum tube thickness was chosen.

Acknowledgements

The authors wish to acknowledge, with thanks, the financial support from the University of Aleppo. Also, the authors wish to express their sincere thanks to Dr. James Carton for his willingness to be a proof reader for this paper.

References

- [1] Olabi AG, Morris E, Hashmi M. Metallic tube type energy absorbers: A synopsis. *Thin-Walled Structures* 2007; 45(7-8):706-726.
- [2] Alghamdi A.A.A. "Collapsible impact energy absorbers: an overview", *Thin-Walled Structures* 2001; 39 (2):189-213.
- [3] DeRuntz Jr JA, Hodge Jr P. Crushing of a tube between rigid plates. *Journal of Applied Mechanics* 1963; 30:391-5.
- [4] Reid S, Reddy TY. Effect of strain hardening on the lateral compression of tubes between rigid plates. *Int.J.Solids Structures* 1978; 14(3):213-225.
- [5] Gupta N, Sekhon G, Gupta P. Study of lateral compression of round metallic tubes. *Thin-walled structures* 2005; 43(6):895-922.
- [6] Yella Reddy T, Reid S. Lateral compression of tubes and tube-systems with side constraints. *Int.J.Mech.Sci.* 1979; 21(3):187-199.
- [7] Reid SR. Laterally compressed metal tubes as impact energy absorbers. In: Jones N, Wierzbicki T, editors. *Structural crashworthiness*. London: Butterworths; 1983. p. 1-43.
- [8] Reid S, Bell W. Influence of strain hardening on the deformation of thin rings subjected to opposed concentrated loads. *Int.J.Solids Structures* 1982; 18(8):643-658.
- [9] Shim, V.P.W.and Stronge, W., (1986), "Lateral crushing of thin-walled tubes between cylindrical indenters", *Int.J.Mech.Sci.*, Vol.28 (10), pp. 683-707.

- [10] Wu L, Carney JF. Experimental analyses of collapse behaviors of braced elliptical tubes under lateral compression. *Int.J.Mech.Sci.* 1998; 40(8):761-777.
- [11] Wu L, Carney JF. Initial collapse of braced elliptical tubes under lateral compression. *Int.J.Mech.Sci.* 1997; 39(9):1023-1036.
- [12] Morris E, Olabi A, Hashmi M. Lateral crushing of circular and non-circular tube systems under quasi-static conditions. *Journal of Materials Processing Tech.* 2007;191(1-3):132-135.
- [13] Morris E, Olabi AG, Hashmi M. Analysis of nested tube type energy absorbers with different indenters and exterior constraints. *Thin-Walled Structures* 2006;44(8):872-885.
- [14] Olabi AG, Morris E, Hashmi M, Gilchrist M. Optimised design of nested oblong tube energy absorbers under lateral impact loading. *Int.J.Impact Eng.* 2008;35(1):10-26.
- [15] Olabi AG, Morris E, Hashmi M, Gilchrist M. Optimised design of nested circular tube energy absorbers under lateral impact loading. *Int.J.Mech.Sci.* 2008;50(1):104-116.
- [16] Hou S, Li Q, Long S, Yang X, Li W. Design optimization of regular hexagonal thin-walled columns with crashworthiness criteria. *Finite Elements in Analysis and Design* 2007;43(6-7):555-65.
- [17] Hou S, Li Q, Long S, Yang X, Li W. Multiobjective optimization of multi-cell sections for the crashworthiness design. *International Journal of Impact Engineering* 2008;35(11):1355-67.
- [18] Zarei H, Kroger M. Bending behavior of empty and foam-filled beams: Structural optimization. *International Journal of Impact Engineering* 2008;35(6): 521-9.

- [19] Chang Qi, Shu Yang, Fangliang Dong. Crushing analysis and multiobjective crashworthiness optimization of tapered square tubes under oblique impact loading. *Thin-Walled Structures* 2012; 59:103-119.
- [20] Thornton P, Mahmood H, Magee C. Energy absorption by structural collapse. *Structural crashworthiness*. e. In: Jones N, Wierzbicki T, editors. *Structural crashworthiness*. London: Butterworths; 1983:96–117.
- [21] Benyounis KY, Olabi AG. Optimization of different welding processes using statistical and numerical approaches – a reference guide. *Adv Eng Software* 2008; 39(6):483–96.
- [22] A. Alaswad , A.G. Olabi, K.Y. Benyounis. Integration of finite element analysis and design of experiments to analyse the geometrical factors in bi-layered tube hydroforming. *Materials and Design* 2011; 32(2): 838–850
- [23] A. Alaswad , K.Y. Benyounis, A.G. Olabi. Employment of finite element analysis and Response Surface Methodology to investigate the geometrical factors in T-type bi-layered tube hydroforming. *Adv Eng Software* 2011; 42(11):917–926.
- [24] Stat-Ease Inc. 'Design-Expert software V8 user's guide', Technical Manual, Stat Ease, Inc., Minneapolis, MN, 2010.
- [25] Montgomery DC. *Design and analysis of experiments*. 2nd ed. New York: Wiley; 1984.

Figure 1: (a) - The tensile test procedure, (b) - True stress–strain curves obtained from tensile tests.

Figure 2: Schematic of an oblong tube sample tube under quasi-static load.

Figure 3: Elongation procedure of an oblong tube.

Figure 4: Tensile force–deflection response of the test piece during the tensile loading phase.

Figure 5: Comparison of load-deflection responses of circular and oblong tubes.

Figure 6: Experimental responses of an FIU system.

Figure 7: (a) Initial and (b) final stages of an FIU system

Figure 8: Experimental responses of an FIIC system.

Figure 9: (a) Initial and (b) final stages of an FIIC system.

Figure 10: Experimental responses of an FISC system.

Figure 11: (a) Initial and (b) final stages of FISC system.

Figure 12: Experimental responses of a CIU system.

Figure 13: Initial and final stages of CIU system.

Figure 14: Experimental responses of a CIIC system.

Figure 15: Initial and final stages of a CIIC system.

Figure 16: Experimental responses of a CISC system

Figure 17: Initial and final stages of a CISC system.

Figure 18: Experimental responses of a PIU system.

Figure 19: (a) Initial and (b) final stages of a PIU system.

Figure 20: Experimental responses of a PIIC system.

Figure 21: Initial and final stages of a PIIC system.

Figure 22: Experimental responses of a PISC system.

Figure 23: Initial and final stages of a PISC system.

Figure 24: The final collapse profile of specimen with a point load application.

Figure 25: Comparison of effectiveness indicators for all systems analysed.

Figure 26: The finite element model of a FIU system

Figure 27: Convergence of crushing force versus mesh density for FIU system

Figure 28: (a) Initial and (b) final deformed shape of the FE model

Figure 29: Comparison of FE & experimental results for an oblong tube

Figure 30: (a) Initial and (b) final deformed shape of FIU numerical model.

Figure 31: Scatter diagram of SEA.

Figure 32: Scatter diagram of F.

Figure 33: Perturbation plot of SEA

Figure 34: Effect of Diameter on SEA

Figure 35: Effect of thickness on SEA.

Figure 36: Variation of SEA with diameter and thickness.

Figure 37: Effect of diameter on F.

Figure 38: Interaction effect of Thickness and width on F

Figure 39: Variation of F with thickness and width.

Figure 40: Overlay plot shows the reign of the optimal working condition

Table 1: Material properties of oblong tubes

Table 2: Comparison of E and SEA for circular and oblong tubes

Table 3: Comparison of FE & experimental results for an oblong tube

Table 4: Independent variables and experimental design levels used.

Table 5: The design matrix.

Table 6: Analysis of variance (ANOVA) table for SEA – Linear model.

Table 7: Analysis of variance (ANOVA) table for F – Quadratic model

Table 8: Confirmation experiment

Table 9: The criterion of numerical optimization

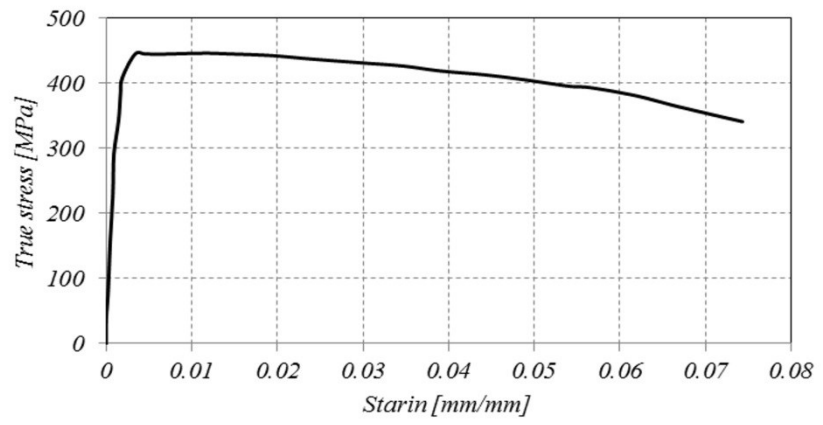
Table 10: Optimal solutions as obtained by Design-Expert

Table 11: Confirmation experiment of optimal solution

Figure 1: (a) - The tensile test procedure, (b) - True stress–strain curves obtained from tensile tests.



a



b

Figure 2: Schematic of an oblong tube sample tube under quasi-static load.

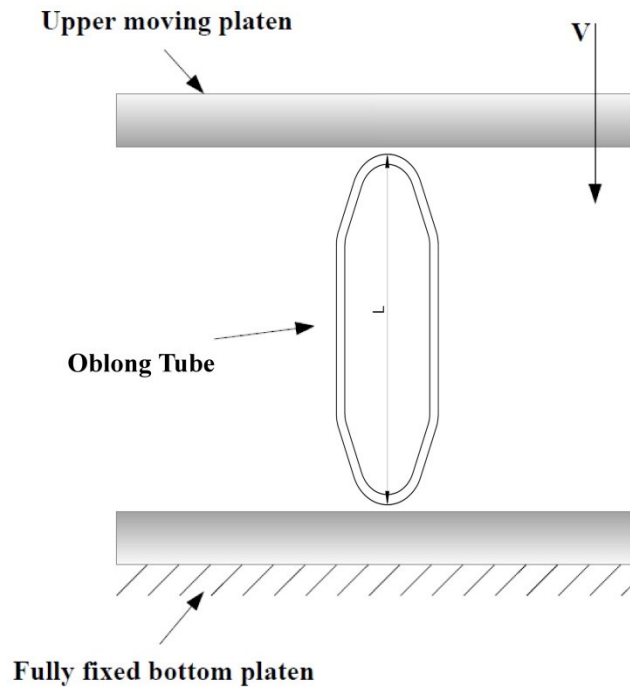


Figure 3: Elongation procedure of an oblong tube.

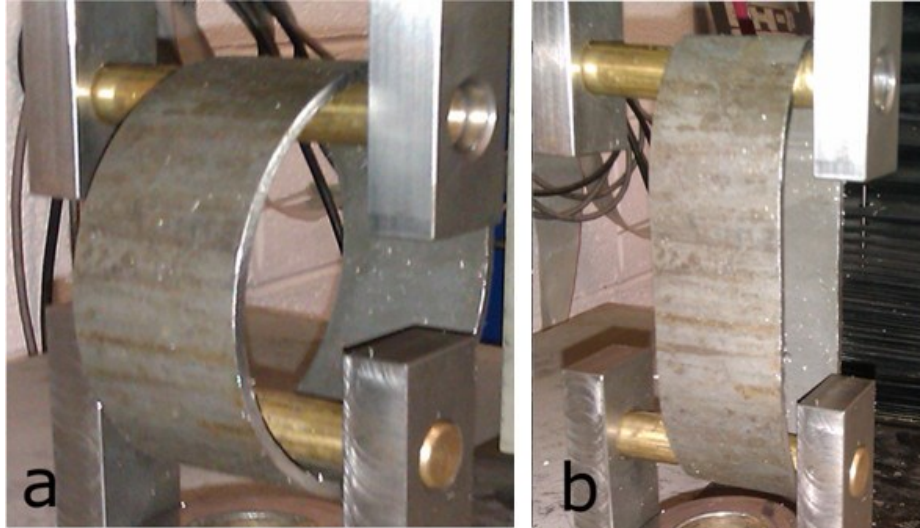


Figure 4: Tensile force–deflection response of the test piece during the tensile loading phase.

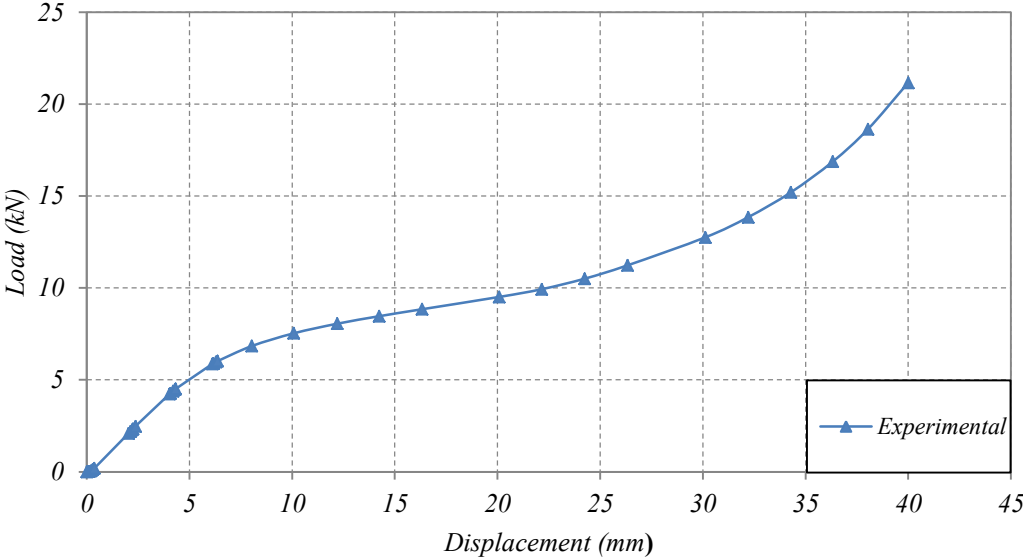


Figure 5: Comparison of load-deflection responses of circular and oblong tubes.

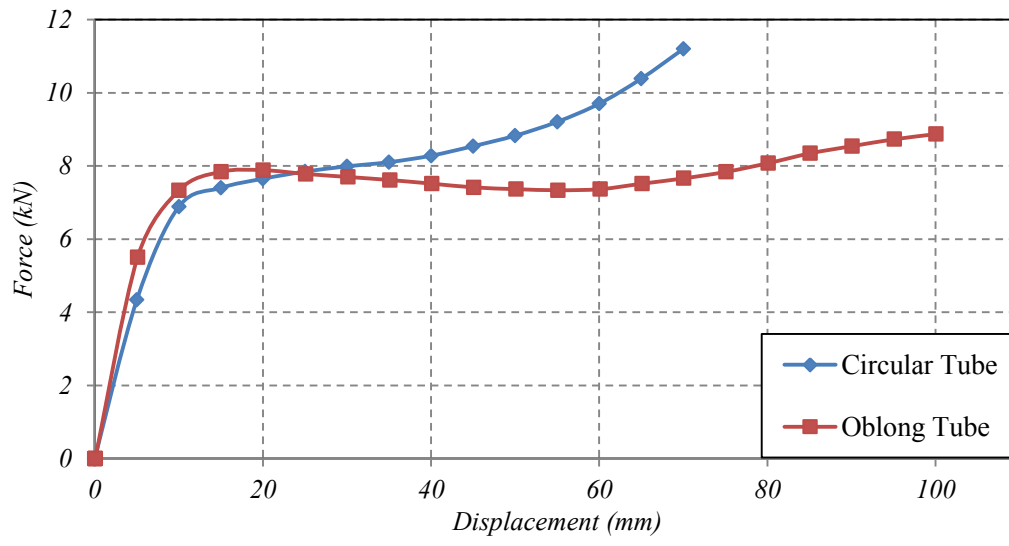


Figure 6: Experimental responses of an FIU system.

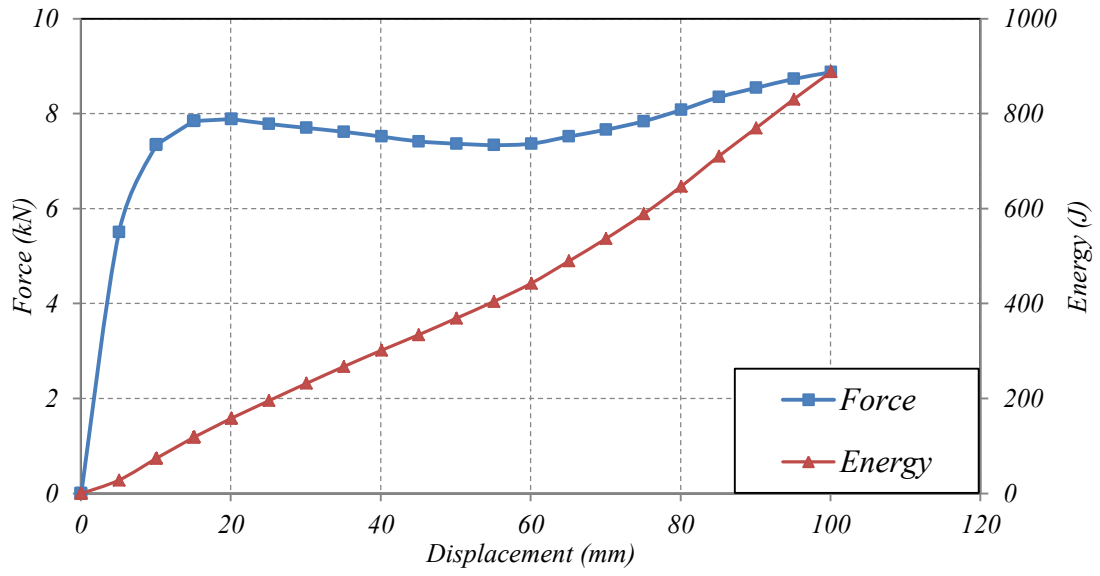


Figure 7: (a) Initial and (b) final stages of an FIU system

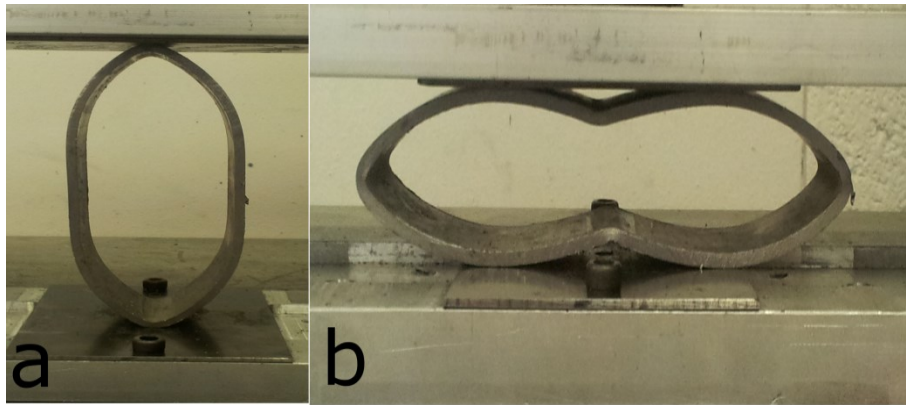


Figure 8: Experimental responses of an FIIC system.

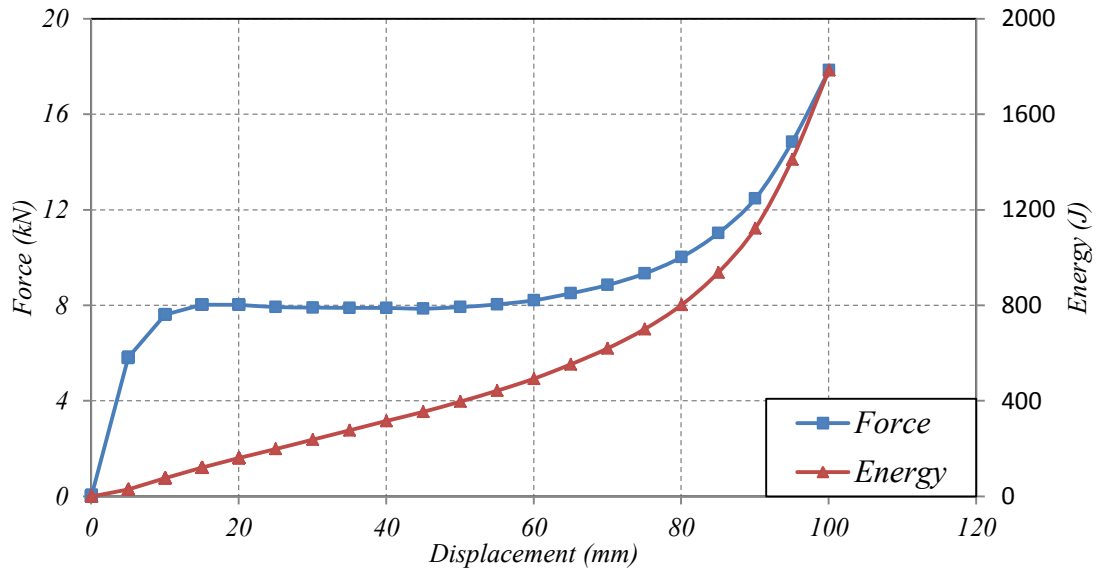


Figure 9: (a) Initial and (b) final stages of an FIIC system.

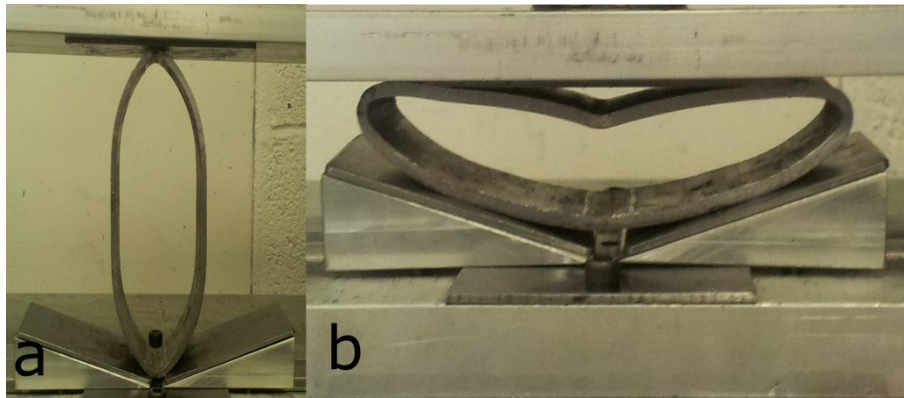


Figure 10: Experimental responses of an FISC system.

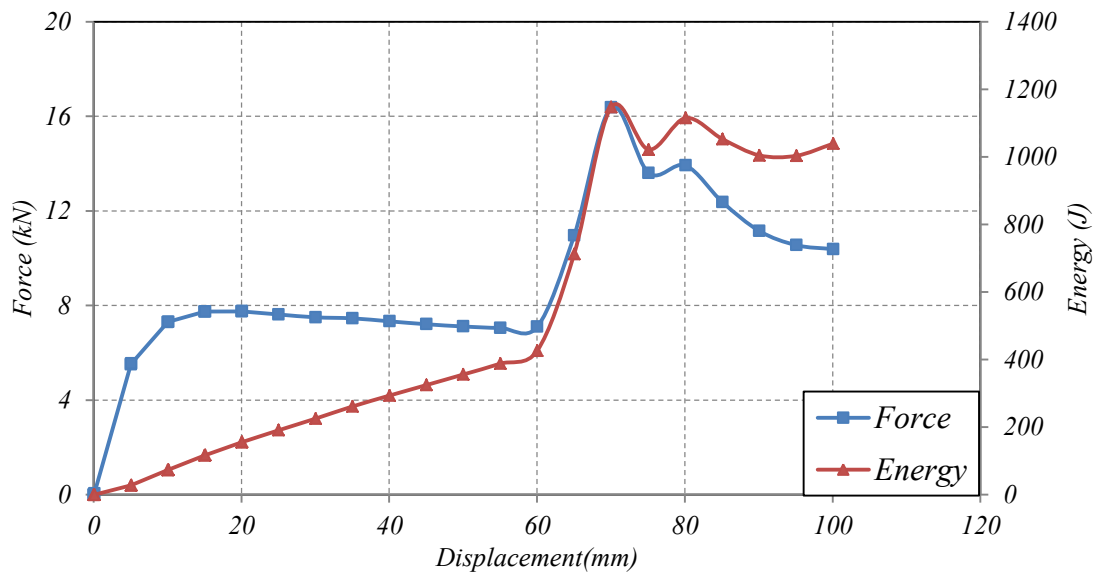


Figure 11: (a) Initial and (b) final stages of FISC system.

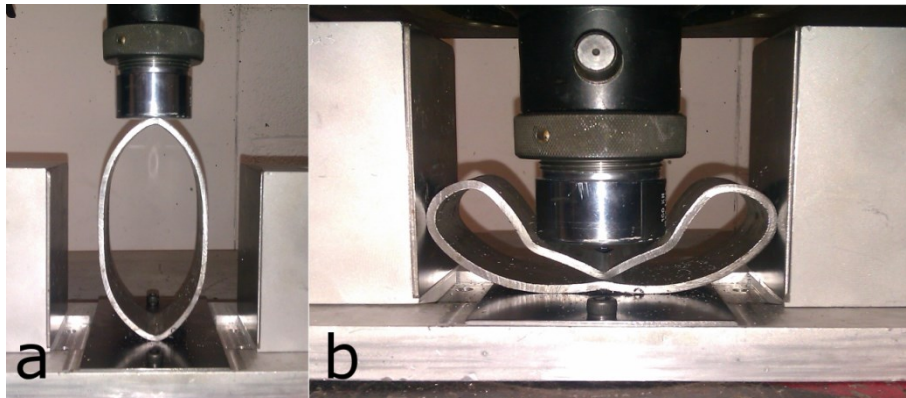


Figure 12: Experimental responses of a CIU system.

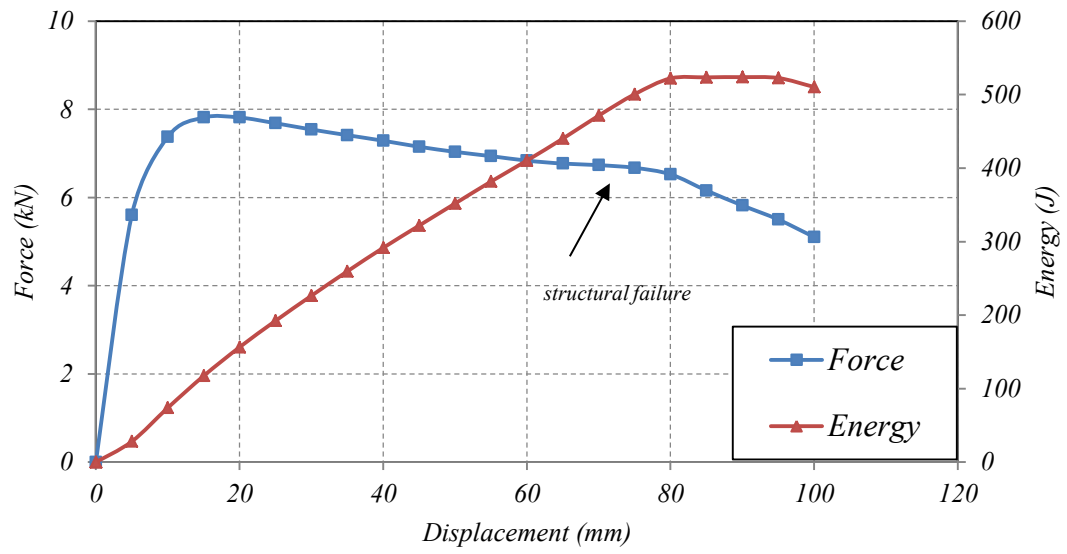


Figure 13: Initial and final stages of CIU system.

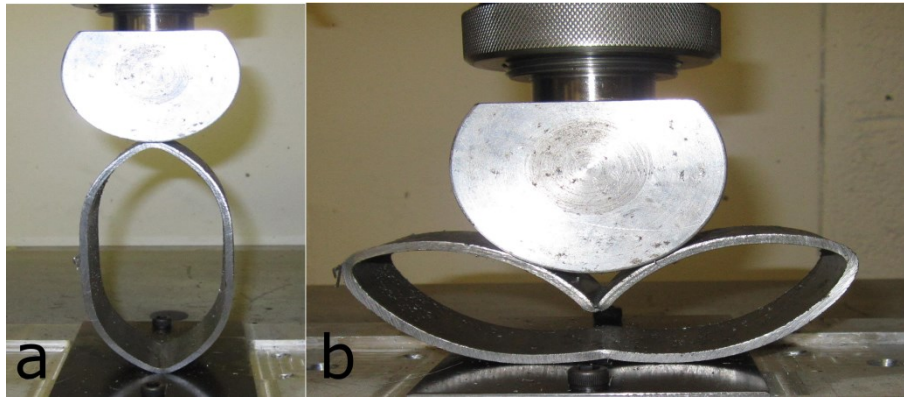


Figure 14: Experimental responses of a CIIC system.

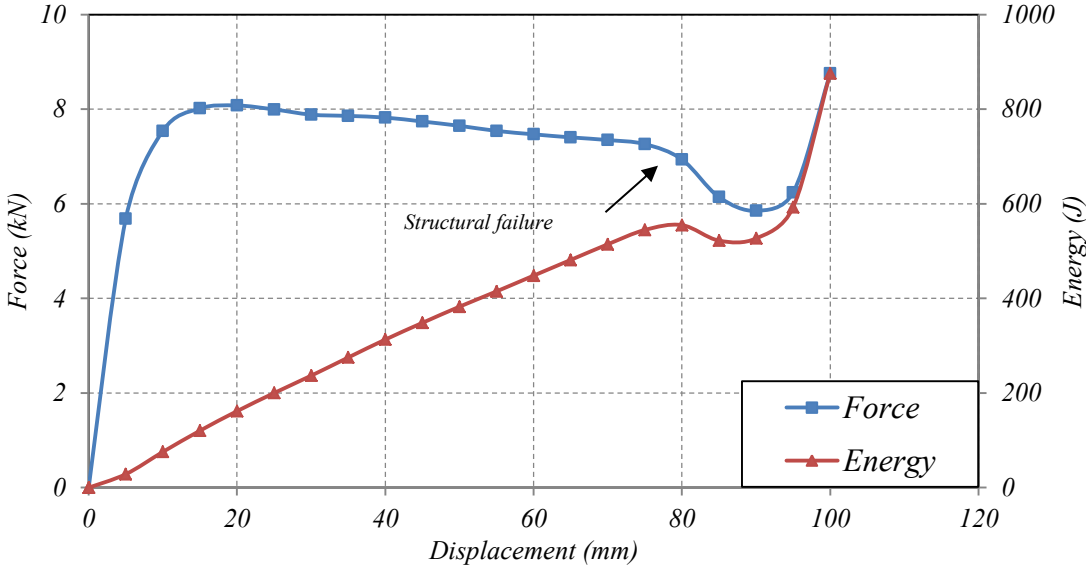


Figure 15: Initial and final stages of a CIIC system.

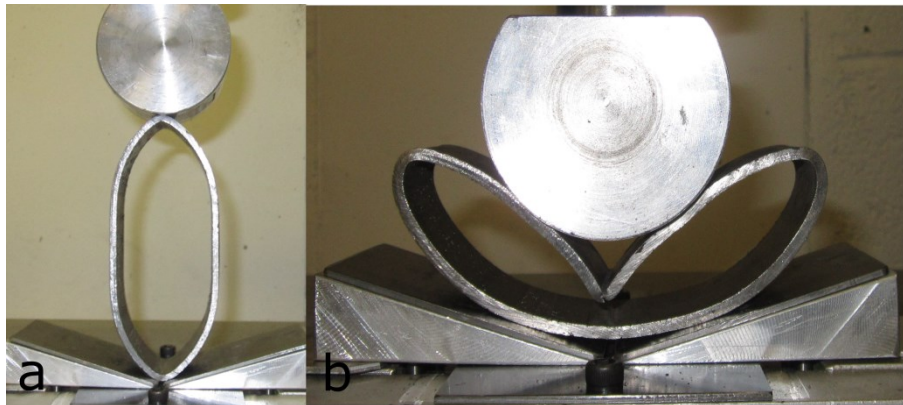


Figure 16: Experimental responses of a CISC system

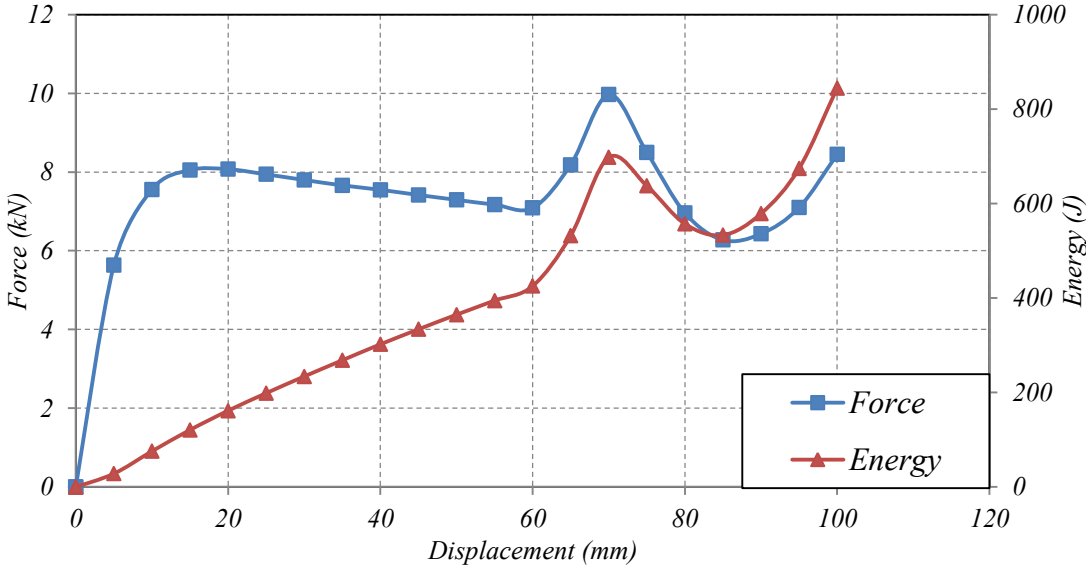


Figure 17: Initial and final stages of a CISC system.

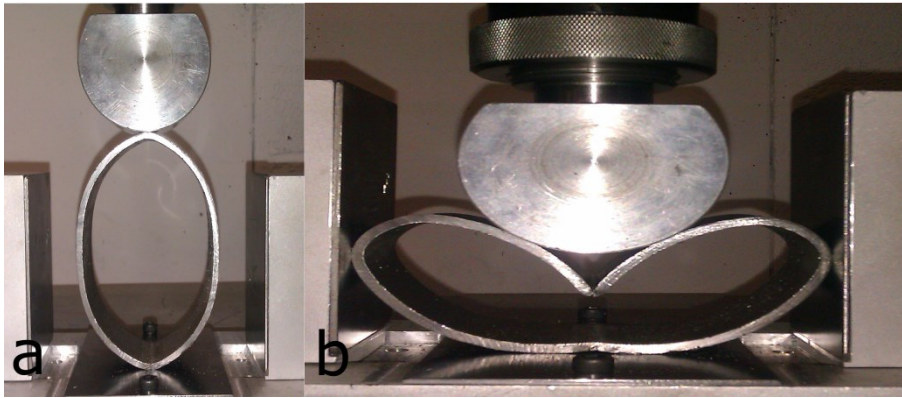


Figure 18: Experimental responses of a PIU system.

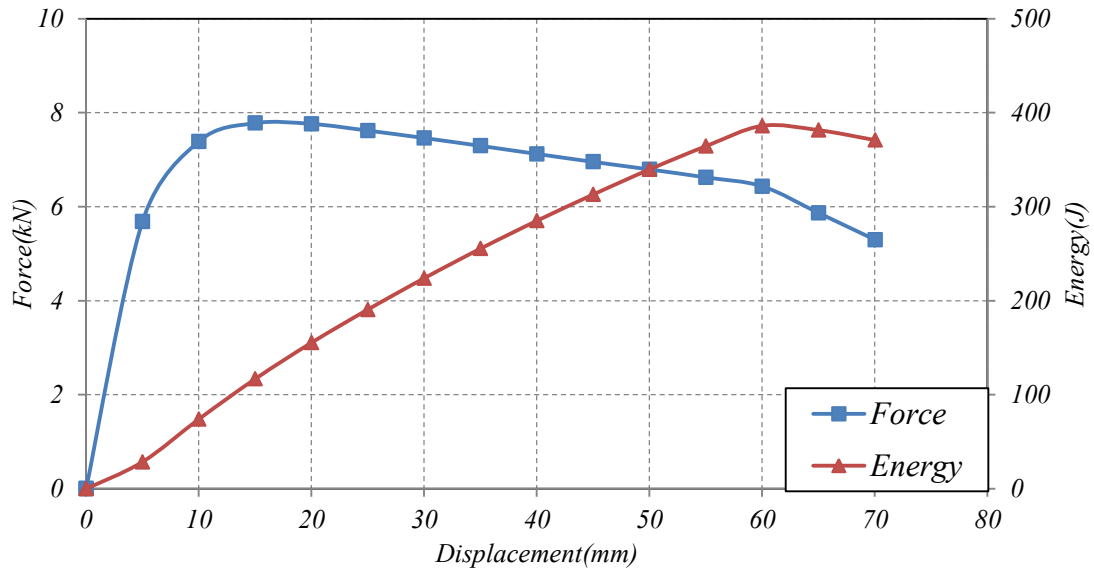


Figure 19: (a) Initial and (b) final stages of a PIU system.

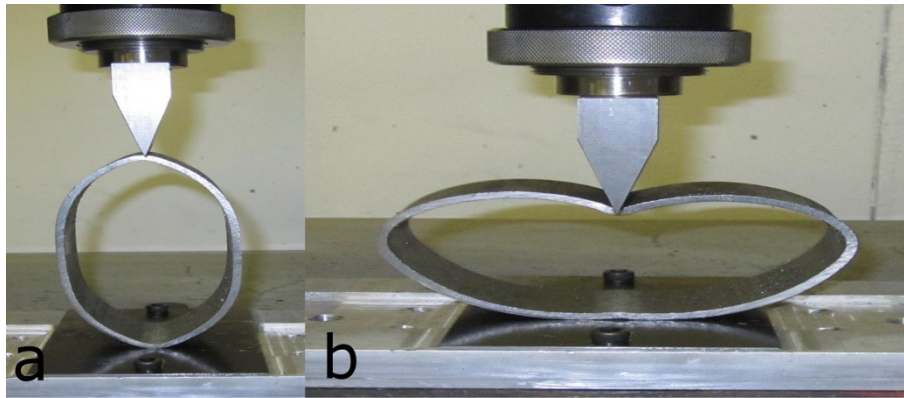


Figure 20: Experimental responses of a PIIC system.

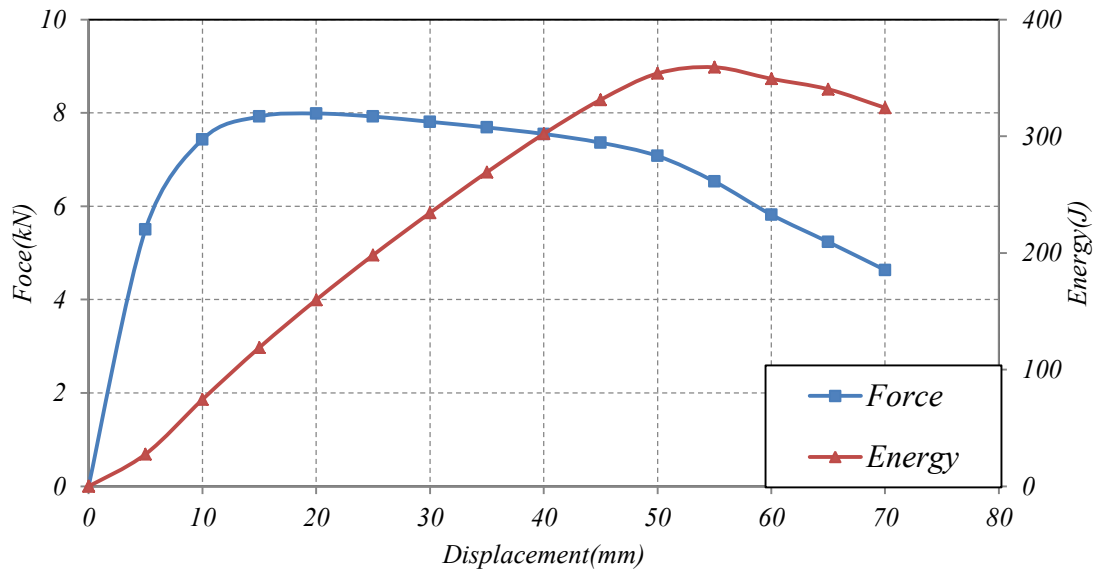


Figure 21: Initial and final stages of a PIIC system.

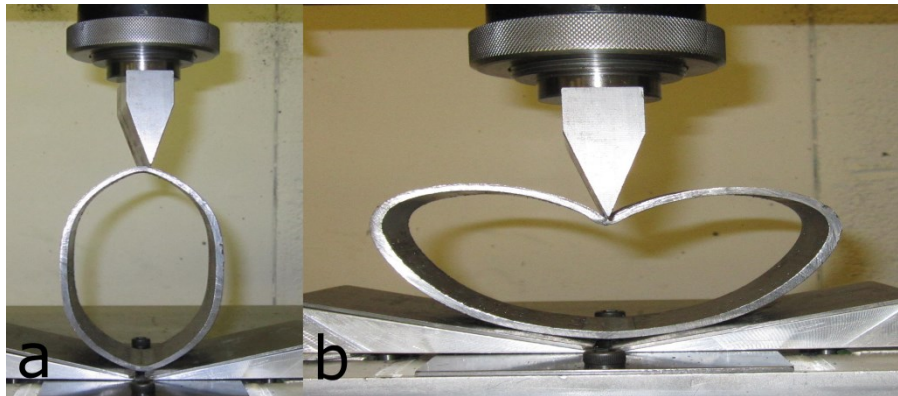


Figure 22: Experimental responses of a PISC system.

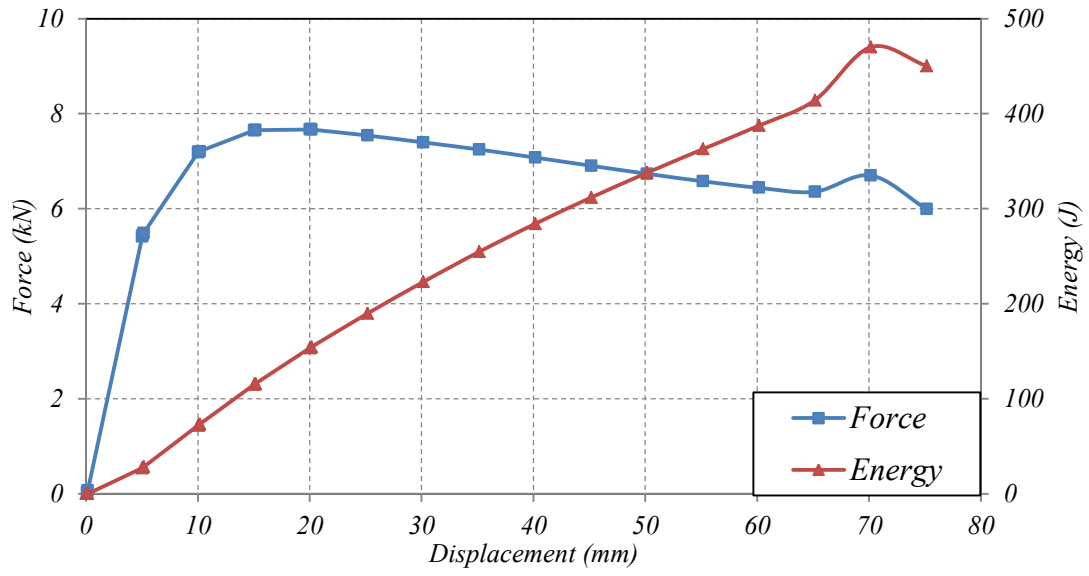


Figure 23: Initial and final stages of a PISC system.

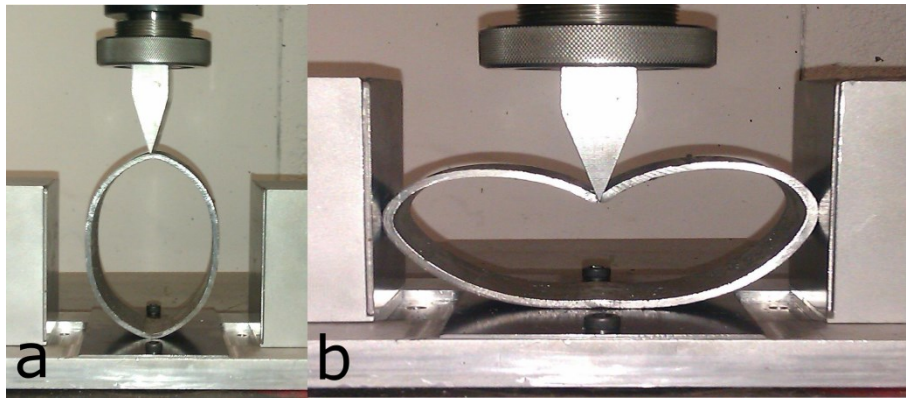


Figure 24: The final collapse profile of specimen with a point load application.



Figure 25: Comparison of effectiveness indicators for all systems analysed.

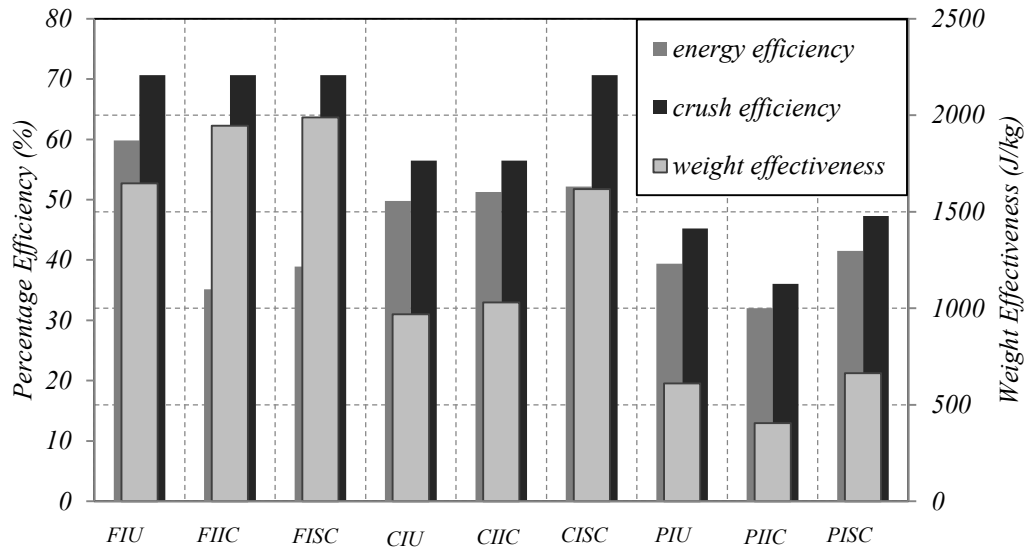


Figure 26: The finite element model of a FIU system

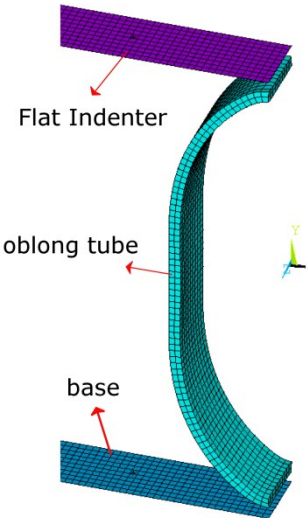


Figure 27: Convergence of crushing force versus mesh density for FIU system

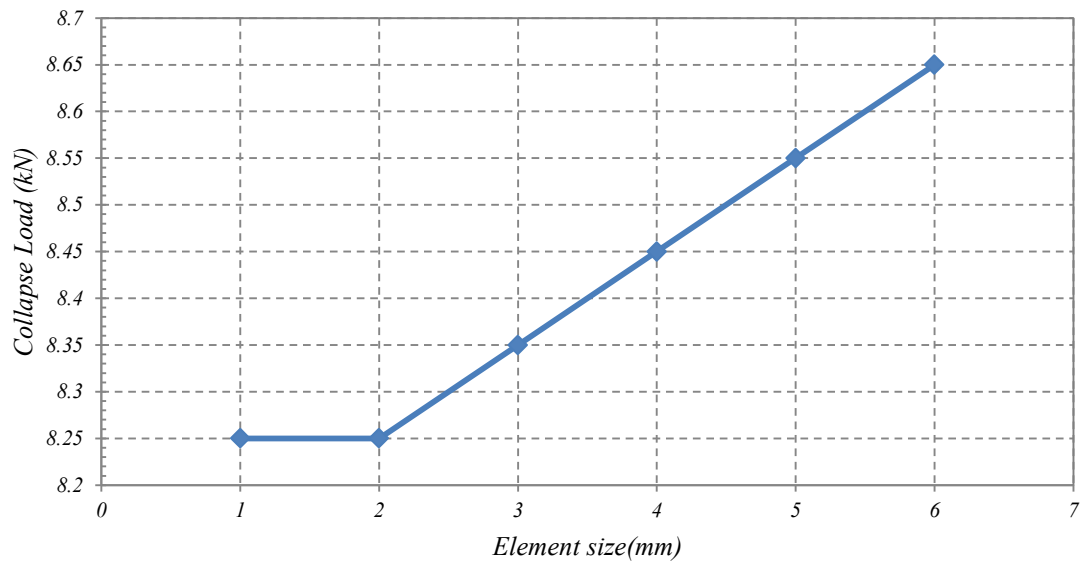


Figure 28: (a) Initial and (b) final deformed shape of the FE model

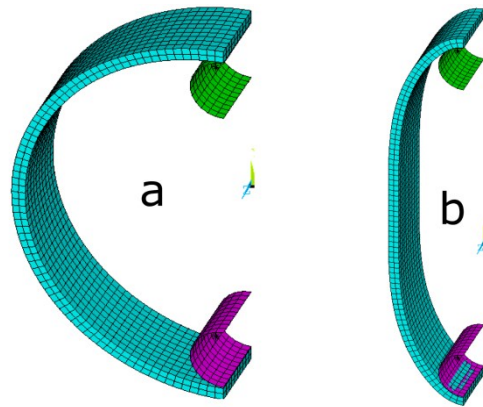


Figure 29: Comparison of FE & experimental results for an oblong tube

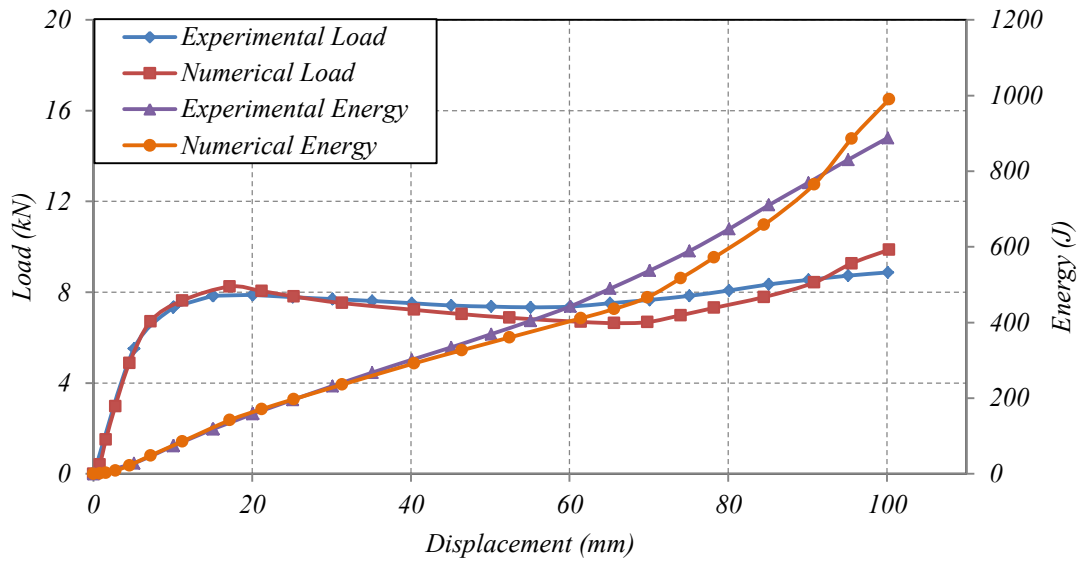


Figure 30: (a) Initial and (b) final deformed shape of FIU numerical model.

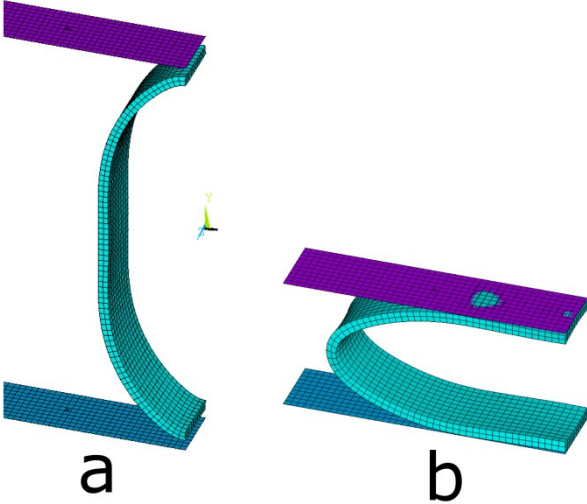


Figure 31: Scatter diagram of SEA.

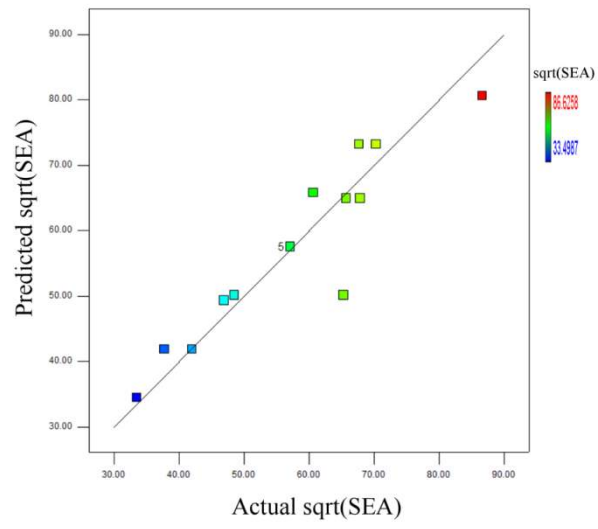


Figure 32: Scatter diagram of F.

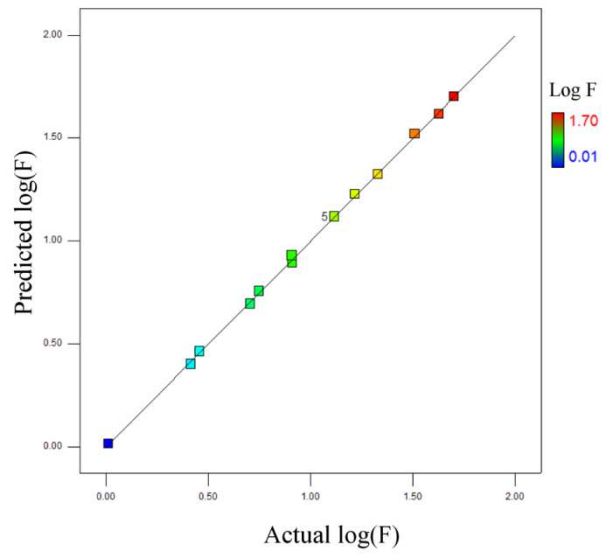


Figure 33: Perturbation plot of SEA

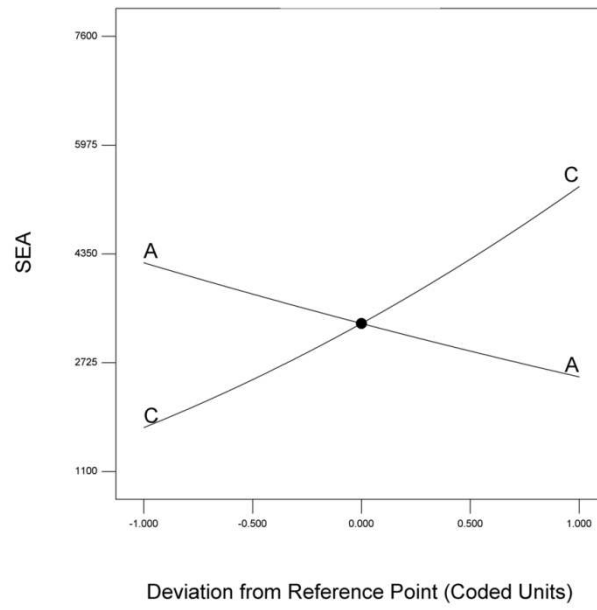


Figure 34: Effect of Diameter on SEA

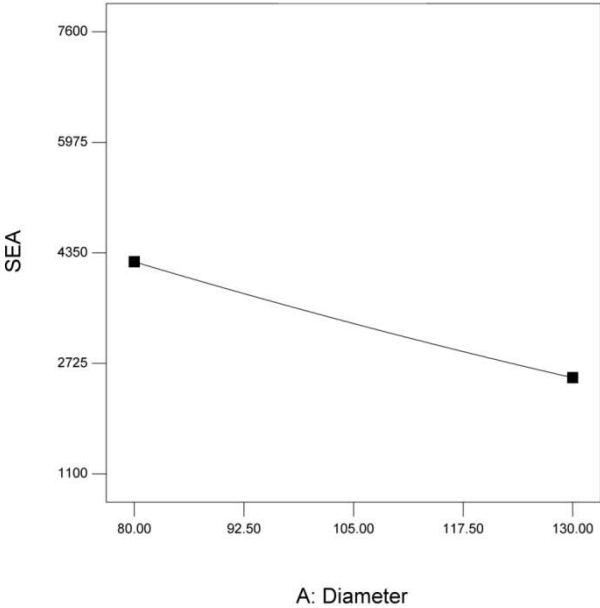


Figure 35: Effect of thickness on SEA.

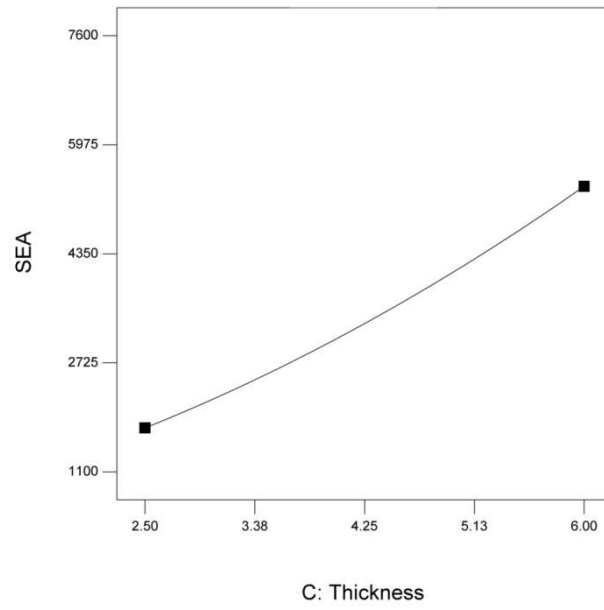


Figure 36: Variation of SEA with diameter and thickness.

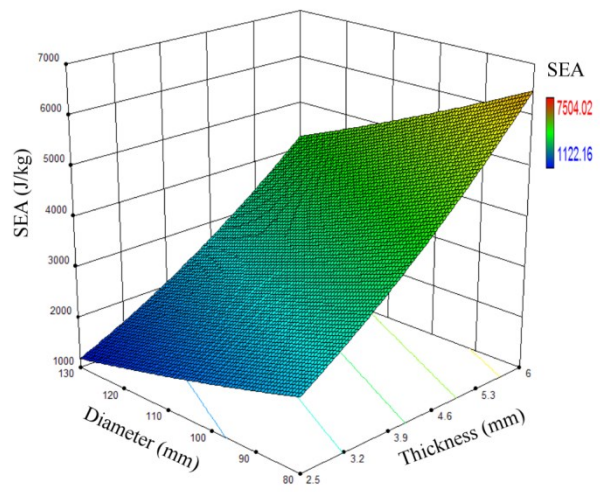


Figure 37: Effect of diameter on F.

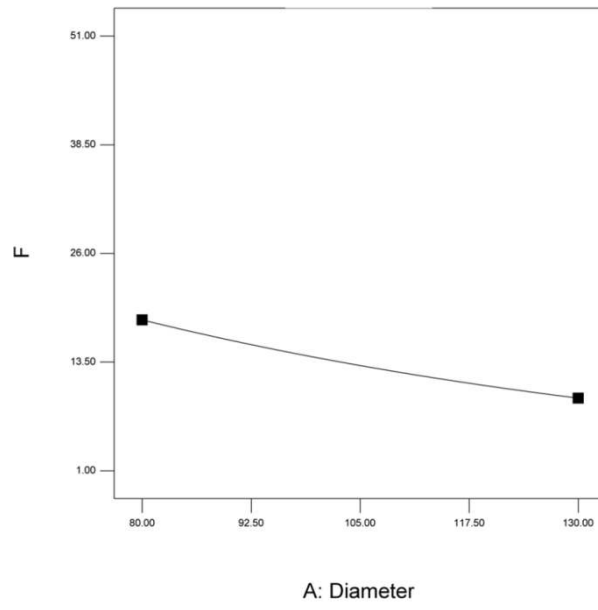


Figure 38: Interaction effect of Thickness and width on F

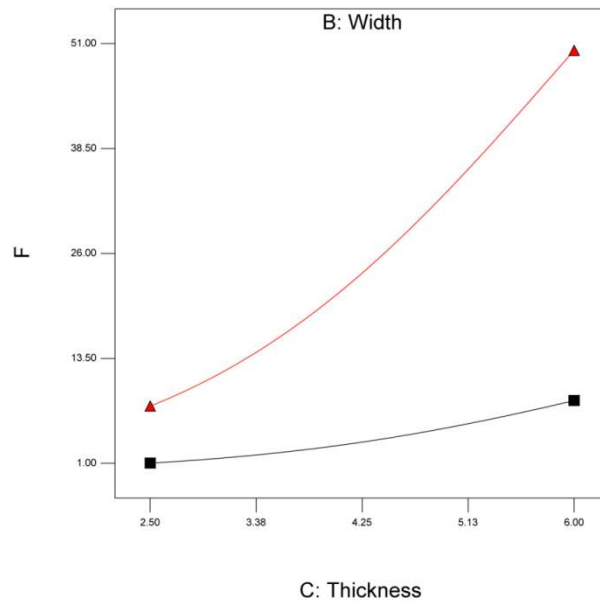


Figure 39: Variation of F with thickness and width.

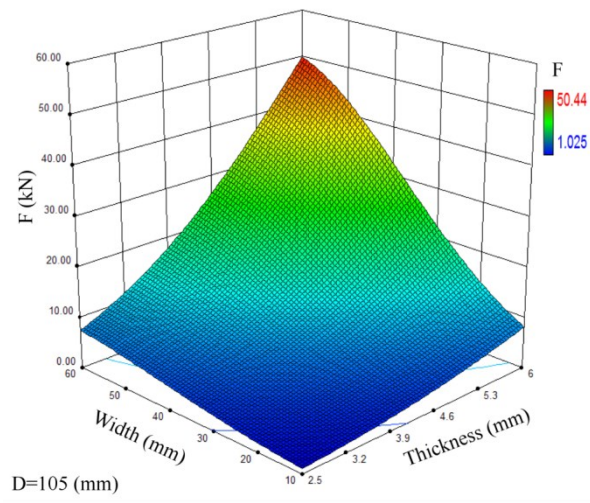


Figure 40: Overlay plot shows the reign of the optimal working condition

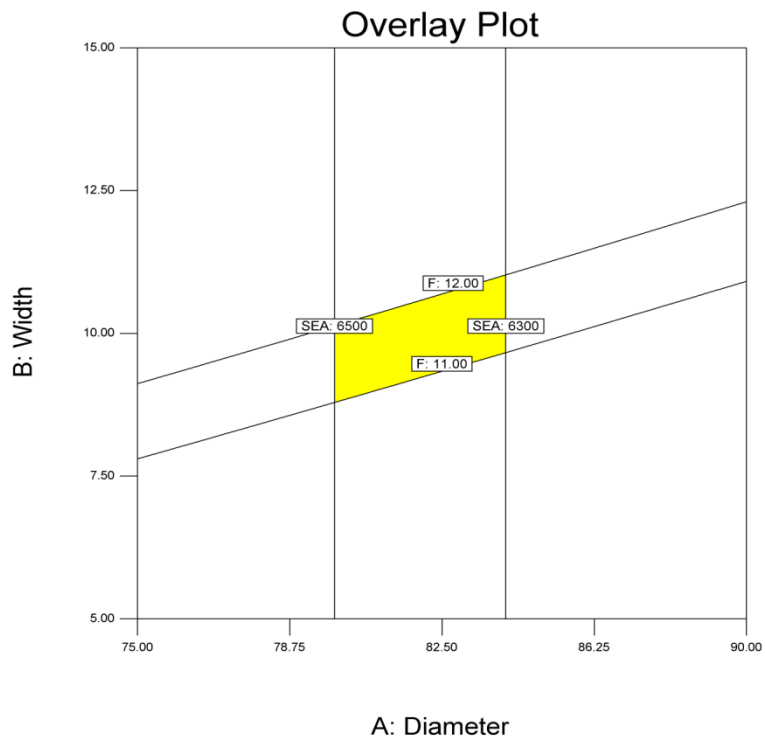


Table 1: Material properties of oblong tubes

	<i>Density</i> (kg/m ³)	<i>Young's modulus</i> (GPa)	<i>Poisson's</i> <i>ratio</i>	<i>Yield strength</i> <i>Rp0.2 (MPa)</i>	<i>Tangent</i> <i>modulus(GPa)</i>
<i>DIN 2393- ST</i> 37.2	7861	200	0.3	470	1.5

Table 2: Comparison of E and SEA for circular and oblong tubes

	E (J)	Mass (kg)	SEA (J/kg)
Oblong	746	0.322	2316.77
Circular	554	0.322	1720.497

Table 3: Comparison of FE & experimental results for an oblong tube

	<i>SEA (J/kg)</i>	<i>F crush (kN)</i>
<i>Experimental</i>	2326.17	8.25
<i>Numerical</i>	2256.01	8.3
<i>Error</i>	3%	0.60%

Table 4: Independent variables and experimental design levels used.

<i>Variable</i>	<i>code</i>	<i>-1</i>	<i>0</i>	<i>1</i>
<i>Diameter(mm)</i>	A	80	105	130
<i>Width(mm)</i>	B	10	35	60
<i>Thickness(mm)</i>	C	2.5	4.25	6

Table 5: The design matrix.

<i>Exp no</i>	<i>D(mm)</i>	<i>W(mm)</i>	<i>t(mm)</i>	<i>SEA (J/kg)</i>	<i>F (kN)</i>
1	80	35	2.5	2200.901	5.6
2	130	60	4.25	2349.348	16.5
3	105	60	2.5	1761.163	8.16
4	105	60	6	4943.279	50.44
5	130	35	6	3678.03	21.43
6	80	35	6	7504.022	42.42
7	80	60	4.25	4604.727	32.378
8	105	35	4.25	3257.608	13.084
9	80	10	4.25	4321.494	5.07
10	105	35	4.25	3257.608	13.084
11	105	10	6	4577.168	8.1
12	105	35	4.25	3257.608	13.084
13	130	10	4.25	4263.601	2.6
14	105	35	4.25	3257.608	13.084
15	130	35	2.5	1122.162	2.86
16	105	10	2.5	1423.097	1.025
17	105	35	4.25	3257.608	13.084

Table 6: Analysis of variance (ANOVA) table for SEA – Linear model.

<i>Source</i>	<i>Sum of squares</i>	<i>Mean Square</i>	<i>F Value</i>	<i>p-value Prob</i>
<i>Model</i>	2395.722442	1197.861221	45.50313719	< 0.0001
<i>A-Diameter</i>	438.4345749	438.4345749	16.65480797	0.0011
<i>C-Thickness</i>	1957.287867	1957.287867	74.3514664	< 0.0001
<i>Residual</i>	368.5472723	26.32480517		
<i>Cor Total</i>	2764.269714			
		<i>Final equation obtained from the model for SEA</i>		
<i>R-Squared</i>	0.8667	$\begin{aligned} \text{Sqrt(SEA)} = &+50.63974 \\ &-0.29612 * \text{Diameter} \\ &+8.93808 * \text{Thickness} \end{aligned}$		
<i>Adj R-Squared</i>	0.8467			
<i>Pred R-Squared</i>	0.7851			
<i>Adeq Precision</i>	21.38			

Table 7: Analysis of variance (ANOVA) table for F – Quadratic model

<i>Source</i>	<i>Sum of Squares</i>	<i>Mean Square</i>	<i>F-Value</i>	<i>P-Value</i>
<i>Model</i>	3.15	0.53	3488.81	< 0.0001
<i>A-Diameter</i>	0.17	0.17	1138.04	< 0.0001
<i>B-Width</i>	1.36	1.36	9051.85	< 0.0001
<i>C-Thickness</i>	1.48	1.48	9834.73	< 0.0001
<i>BC</i>	2.85E-03	2.85E-03	18.88	0.0015
<i>B²</i>	0.1	0.1	682.22	< 0.0001
<i>C²</i>	0.025	0.025	166.87	< 0.0001
<i>Residual</i>	1.51E-03	1.51E-04		
<i>Cor Total</i>	3.16			
<i>Final equation obtained from the model for F</i>				
<i>R-Squared</i>	0.9995	$\text{Log}_{10}(F) =$ $-0.74264 - 5.85586E-003 * \text{Diameter} + 0.036580 * \text{Width}$ $+ 0.48143 * \text{Thickness} - 6.09578E-004 * \text{Width} * \text{Thickness}$ $2.49636E-004 * \text{Width}^2 - 0.025197 * \text{Thick}^2$		
<i>Adj R-Squared</i>	0.9992			
<i>Pred R-Squared</i>	0.9969			
<i>Adeq Precision</i>	214.12			

Table 8: Confirmation experiment

<i>D(mm)</i>	<i>t (mm)</i>	<i>w(mm)</i>		<i>SEA (J/kg)</i>	<i>F (kN)</i>
101.6	3.25	40	<i>Experimental</i>	2326.17	8.25
			<i>Numerical (FEM)</i>	2256.01	8.3
			<i>Error (%)</i>	3%	0.60%
			<i>Predicted (RSM)</i>	2460.431	8.82
			<i>Error (%)</i>	9%	6.2%

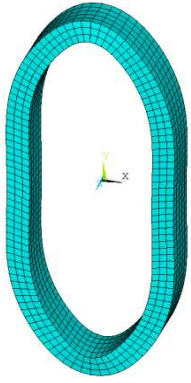
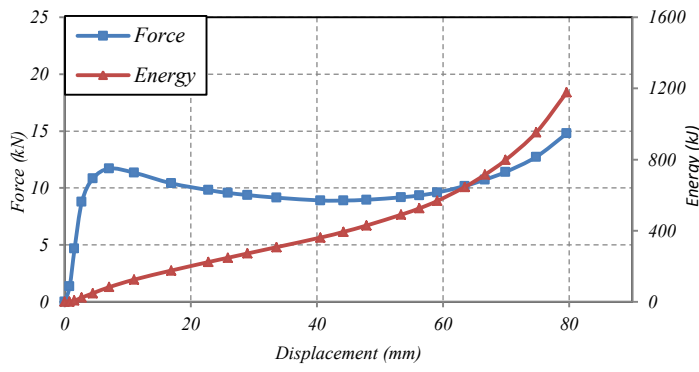
Table 9: The criterion of numerical optimization

<i>Name</i>	<i>Goal</i>	<i>lower Limit</i>	<i>Upper Limit</i>	<i>Weight</i>	<i>Importance</i>
<i>D (mm)</i>	is in range	80	130	1	3
<i>t (mm)</i>	is in range	10	60	1	3
<i>W (mm)</i>	is in range	2.5	6	1	3
<i>SEA (J/kg)</i>	maximize	1122.16	7504	10	3
<i>F (kN)</i>	minimize	1.025	50.44	1	3

Table 10: Optimal solutions as obtained by Design-Expert

<i>Number</i>	<i>Diameter(mm)</i>	<i>Width(mm)</i>	<i>Thickness(mm)</i>	<i>SEA(J/kg)</i>	<i>F(kN)</i>	<i>Desirability</i>
1	80	10	6	6492.91	11.88	0.31
2	80	10.27	6	6492.87	12.08	0.309
3	80	10.84	6	6490.09	12.52	0.307
4	80	11.53	6	6492.92	13.08	0.306
5	80	11.81	6	6492.92	13.31	0.306

Table 11: Confirmation experiment of optimal solution

	<i>SEA (J/kg)</i>	<i>F (kN)</i>																																	
<i>Numerical (FE)</i>	6821.4	11.71																																	
<i>Predicted (RSM)</i>	6492.917	11.81																																	
<i>Error</i>	4.80%	0.85%																																	
<i>Geometry</i>	<i>Force and energy responses of optimal configuration</i>																																		
	 <table border="1"> <caption>Data points estimated from the Force and Energy graph</caption> <thead> <tr> <th>Displacement (mm)</th> <th>Force (kN)</th> <th>Energy (kJ)</th> </tr> </thead> <tbody> <tr><td>0</td><td>0</td><td>0</td></tr> <tr><td>5</td><td>11</td><td>100</td></tr> <tr><td>10</td><td>12</td><td>200</td></tr> <tr><td>20</td><td>10</td><td>400</td></tr> <tr><td>30</td><td>9</td><td>600</td></tr> <tr><td>40</td><td>9</td><td>800</td></tr> <tr><td>50</td><td>9</td><td>1000</td></tr> <tr><td>60</td><td>10</td><td>1200</td></tr> <tr><td>70</td><td>12</td><td>1400</td></tr> <tr><td>80</td><td>15</td><td>1600</td></tr> </tbody> </table>		Displacement (mm)	Force (kN)	Energy (kJ)	0	0	0	5	11	100	10	12	200	20	10	400	30	9	600	40	9	800	50	9	1000	60	10	1200	70	12	1400	80	15	1600
Displacement (mm)	Force (kN)	Energy (kJ)																																	
0	0	0																																	
5	11	100																																	
10	12	200																																	
20	10	400																																	
30	9	600																																	
40	9	800																																	
50	9	1000																																	
60	10	1200																																	
70	12	1400																																	
80	15	1600																																	